

## Analysis of a Convective Storm Crossing Poyang Lake in China

Haibo ZOU<sup>1,2</sup>, Shuwen ZHANG<sup>1\*</sup>, Yanan LIU<sup>2</sup>, Weidong ZHANG<sup>1</sup>, and Xixi YANG<sup>1</sup>

<sup>1</sup> College of Atmosphere Sciences, Lanzhou University, Lanzhou 730000

<sup>2</sup> Institute of Meteorological Sciences of Jiangxi Province, Jiangxi Meteorological Bureau, Nanchang 330046

(Received September 10, 2019; in final form February 5, 2020)

### ABSTRACT

A convective storm crossing Poyang Lake (PL) in China during 1200–1600 UTC on 13 May 2015 is examined. The results show that this storm occurs ahead of a 500-hPa trough with weak low-level temperature advection and a convectively stable layer between 925 and 850 hPa, and the tail of the storm is enhanced when its spearhead sweeps over PL after the sunset. Due to the heating and moistening of PL, the convectively stable layer over PL is destabilized; and instead, a deep (below 700 hPa) convectively unstable layer is organized. Moreover, both the radiative cooling and the storm-induced cooling result in a rapid air (near-surface) and land temperature decrease in the surrounding areas. Thus, a large lake–land temperature difference (about 6°C) occurs, which is conducive to generating land–lake breeze and enhancing the convergence of the low-level wind. Finally, the PL-induced deep convectively unstable layer and the enhanced low-level convergence jointly strengthen the crossing storm. To further confirm this, two simulations (with or without PL) are conducted with the Weather Research and Forecast (WRF) model. The simulation with PL successfully reproduces the evolution of the storm crossing PL, while the simulation without PL fails. In the simulation with PL, a high  $\theta_{se}$  tongue at 850 hPa associated with the storm moves eastward and downward, and merges with the PL-induced lake boundary layer, forming a deep convectively unstable layer under 700 hPa. However, in the simulation without PL, the stable layer constantly maintains under 900 hPa. In addition, the 900-hPa wind difference between the simulations with and without PL shows a land–lake breeze circulation that strengthens the convergence of the low-level wind.

**Key words:** Poyang Lake (PL), lake-enhanced precipitation, lake–land breeze, convective instability

**Citation:** Zou, H. B., S. W. Zhang, Y. N. Liu, et al., 2020: Analysis of a convective storm crossing Poyang Lake in China. *J. Meteor. Res.*, **34**(3), 529–545, doi: 10.1007/s13351-020-9143-5.

## 1. Introduction

Due to the large difference of specific heat capacity between water and land, lake can significantly influence the weather and climate in its vicinity (Petterssen and Cabarese, 1959). The most famous effect is the well-known lake-effect precipitation (including snow). The lake can trigger precipitation over the lake and on its downwind side under certain conditions (Moore and Orville, 1990). Wiggin (1950) pioneered the forecasting skills for lake-effect precipitation in the western New York. Holroyd (1971), Dockus (1985), and others improved the predictability of lake-effect precipitation over the Great Lakes (all individual lakes cover more than 10,000 km<sup>2</sup>) in

North America. Later, Schoenberger (1986), Byrd et al. (1991), Miner and Fritsch (1997), Laird (1999), Ruhf and Cutrim (2003) as well as Kristovich and Spinar (2005) studied the climatic characteristics, morphologies, and ambient conditions of lake-effect precipitation over the Great Lakes. They emphasized that the vertical temperature difference between the lake and 700 or 850 hPa can approach the dry-adiabatic lapse rate and plays a key role in the development of lake-effect precipitation. They also found that the lake-effect events usually occur under strong low-level cold temperature advection shortly after a cold front passes. Besides, Hjelmfelt (1990), Ballentine et al. (1993), and Wright et al. (2013) have used numerical models to further understand how the Great

Supported by the National Natural Science Foundation of China (41865003, 41575098, and 41765001) and Jiangxi Provincial Department of Science and Technology Project (2017BBG70004).

\*Corresponding author: zhangsw@lzu.edu.cn.

©The Chinese Meteorological Society and Springer-Verlag Berlin Heidelberg 2020

Lakes could contribute to local lake-effect precipitation.

Studies found that there also exists obvious lake-effect precipitation over the middle- and small-size lakes (water coverage less than 5000 km<sup>2</sup> or even 1000 km<sup>2</sup>), such as the Great Salt Lake with an area of about 4400 km<sup>2</sup> (Steenburgh et al., 2000; Alcott et al., 2012), Champlain Lake with an area of about 1200 km<sup>2</sup> (Laird et al., 2009), Finger Lakes with an area of approximately 1000 km<sup>2</sup> (Laird et al., 2010), Tahoe Lake (approximately 500 km<sup>2</sup>) and Pyramid Lake (approximately 500 km<sup>2</sup>) in North America (Laird et al., 2016), and Taihu Lake with an area of approximately 2400 km<sup>2</sup> in China (Gu et al., 2016). Importantly, Steenburgh et al. (2000) reported that the large lake–land temperature difference (usually more than 6°C) is conducive to generating obvious land–lake breeze, which can make the low-level air heated and moistened by the lake convergence toward the lake center, and trigger the lake-effect event. Alcott et al. (2012) claimed that the temperature lapse rate is only needed to be greater than the moist-adiabatic lapse rate instead of the dry-adiabatic lapse rate in the near-saturated ambient atmosphere for the lake-effect precipitation.

In addition to the lake-effect precipitation (directly triggered precipitation by lakes), lake can also influence the existing storms passing through it, and the impact (strengthening or weakening) largely depends on the lake–land temperature difference. In wintertime when the lake surface is warmer than the surrounding land surface, lake can not only significantly strengthen the convection originated from an upstream lake (Rose, 2001; Rodriguez et al., 2007; Kristovich et al., 2018; Lang et al., 2018), but also increase the precipitation and change the moving speed of synoptic cyclones crossing the Great Lakes (Angel and Isard, 1998; Schroeder et al., 2006; Owens et al., 2017). The enhancement of the crossing storm is mainly caused by the fact that lake can increase the surface temperature and dewpoint temperature, and reduce the low-level stability under the intense cold temperature advection (Schroeder et al., 2006; Owens et al., 2017). However, in summertime when the lake surface is cooler than the surrounding land surface, the majority of storms crossing lakes tend to be weakened (Metz, 2011; Workoff et al., 2012). Besides, the low-level vertical wind shear over the lake could also impact the crossing storm (Lombardo and Colle, 2012; Workoff et al., 2012).

Poyang Lake (PL) is the largest seasonal freshwater lake in China, with about 3800 km<sup>2</sup> of water coverage in summertime, and can obviously affect the local weather and climate. For example, PL can warm the overlying air during the nighttime (heat source) in summer while cool-

ing the overlying air during the daytime (cold source) due to the relatively shallow water depth (Wan et al., 1994). Owing to the noteworthy heating or cooling, PL and its adjacent areas present an obvious lake–land breeze circulation in summertime (Cao et al., 2015). Fu et al. (2013) found that a convective system weakened and dissipated when it crossed over PL during the daytime on 23 July 2007. Xu et al. (2006) indicated that when Typhoon Rananim passed through PL in August 2004, the upward motion and divergence fields showed the signals to enhance the local rainfall.

However, there are few studies reporting the enhancement of crossing convective storms over PL. Besides, the enhancement could be monitored by China New Generation Weather Radar (CINRAD) in Nanchang (NANC) occasionally. On 13 May 2015, a convective storm strengthened when crossing PL during the nighttime. In this study, we carefully investigate how PL strengthens the crossing convective storm using both observations and simulations, and provide related physical explanations. The remainder of this paper is organized as follows. Section 2 describes PL and the data used in this study. Section 3 presents the evolution of the storm, and Section 4 depicts the simulation. Conclusions are given in Section 5.

## 2. Study domain and data

### 2.1 PL and its surrounding topography

PL is located in the north of Jiangxi Province in East China and next to the south bank of the Yangtze River (Fig. 1a). Its shape and size are similar to those of the Great Salt Lake in the western America, but the location of PL is more than 1000 km south of the Great Salt Lake. PL occupies an area of approximately 3800 km<sup>2</sup>, with length of about 130 km, average width of about 30 km (the maximum width is approximately 75 km), and mean depth of less than 6 m in summer (Shankman et al., 2012; Li et al., 2017). The major axis of the lake orients from northwest to southeast (Fig. 1b). A steeply sloped mountain (Mufu Mountain) with an altitude exceeding 800 m is located to the west of PL (Fig. 1b). NANC City, the capital of Jiangxi Province, is located approximately 30 km to the southwest of PL, with its urban area of about 900 km<sup>2</sup> (see the biggest carnation-color region in Fig. 1b). Several counties [Yongxiu (YX), Dean (DA), Duchang (DC), Poyang (PY), and Jinxian (JX)] are also situated around PL, with the individual urban area less than 25 km<sup>2</sup> (Fig. 1b). There are two low hills of approximately 100-m altitude between NANC City and YX County. The Ganjiang River passes through NANC City

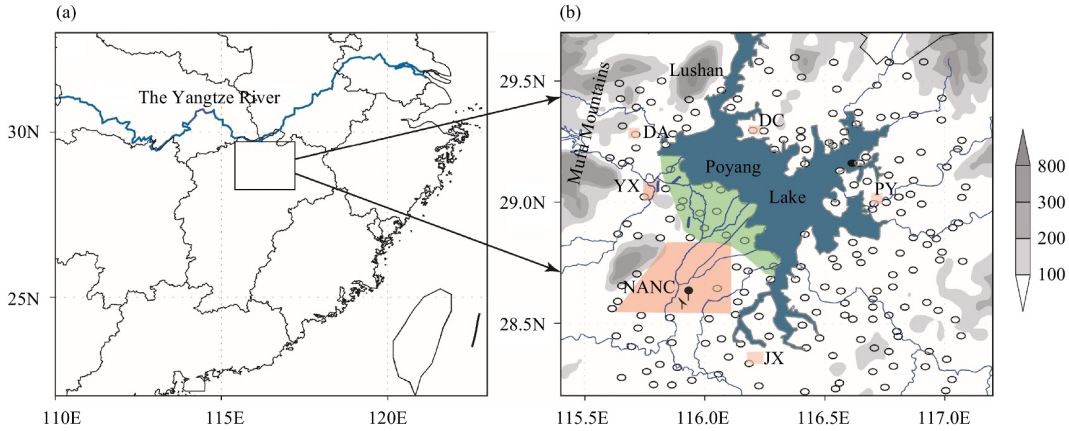


**Fig. 1.** (a) The location of PL in East China. (b) The area of PL (blue shaded), and the surrounding topography (gray shaded; m; see color bar on the right), the temperature and rainfall observation stations (open circles), the sensible heat flux observation station (the solid circle) on the east shore of PL, and the radar and sounding stations in Nanchang (NANC) City. The regions in carnation (green) color are urban (wetland) areas. The blue lines in (a) and (b) denote rivers.

and is divided into several smaller tributaries flowing into the west of PL. Owing to the low altitude and the abundant water resource, a large wetland appears to the west of PL (Fig. 1b).

## 2.2 Data

### 2.2.1 Data sources

In the region around PL, there are 190 automatic rainfall and temperature observation stations, one Doppler radar, one sounding station, and one open-path eddy covariance observation station that can measure sensible and latent heat fluxes. The data obtained from these instruments are provided by the Meteorological Information Center of Jiangxi Province in China and can be accessed from the Meteorological Unified Service Interface Community system through the Intranet of Jiangxi Meteorological Administration. Both the Doppler radar (CINRAD S-band with type of A, namely CINRAD-SA, which is similar to Weather Surveillance Radar 88 Doppler in America) and the sounding station are located in NANC City (Fig. 1b). The open-path eddy covariance instrument EC150 (including a CAST3 3D ultrasonic anemometer with a 10-Hz sample frequency) is installed at 44 m on a 70-m tower in a small island on the east shore of PL (Fig. 1b; solid circle). The distance from the tower to the water surface of PL is less than 10 m and the terrain around the tower is flat (the height is less than 2 m) (Wang et al., 2016). The moderate resolution imaging spectroradiometer (MODIS) land surface temperature (MYD11A1) data are achieved from NASA. The 6-h ECMWF reanalysis (ERA)-interim data are obtained from the ECMWF with a horizontal resolution of  $0.25^\circ \times 0.25^\circ$ . The NCEP final operational global analysis data (FNL) with a horizontal resolution of  $1^\circ \times 1^\circ$  are used to

drive the Weather Research and Forecasting (WRF) model.

### 2.2.2 Data processing

The radar volume scan (level II) data of NANC is measured by the volume coverage pattern (VCP) 21 mode that includes 9 elevation angles ( $0.58^\circ$ ,  $1.58^\circ$ ,  $2.48^\circ$ ,  $3.48^\circ$ ,  $4.38^\circ$ ,  $6.08^\circ$ ,  $9.98^\circ$ ,  $14.68^\circ$ , and  $19.58^\circ$ ), and stored in the format of polar coordinates with a 1-km resolution in range and an about  $1^\circ$  resolution in azimuth (Zou et al., 2019). The radar data are firstly quality controlled to remove non-meteorological echoes by using an improved quality-control method for radar reflectivity (Zou et al., 2018), and then converted into a Cartesian coordinate with a horizontal resolution of  $0.01^\circ \times 0.01^\circ$  by the nearest-neighbor interpolation method on the range–azimuth plane (Xiao et al., 2008).

Lake temperature is an important factor for the lake-effect and lake-enhanced events (Carpenter, 1993; Miner and Fritsch, 1997; Laird et al., 2010, 2016; Metz, 2011). It not only indicates the amount of energy available in a lake that is transferrable to the lowest layers of the atmosphere to enhance the instability, but also determines the maximum saturation vapor pressure of the overlying air mass (Carpenter, 1993). Since there are no lake temperature measurements in PL, the sensible heat flux observation (EC150) is used to retrieve the lake surface temperature. The retrieving method is as follows (Lu et al., 1988):

$$H_s = \rho C_p C_H U_{10} (T_{10} - T_s), \quad (1)$$

where  $\rho$  is the air density,  $C_p = 1004.67 \text{ J kg}^{-1} \text{ K}^{-1}$  is the specific heat at constant pressure,  $U_{10}$  ( $T_{10}$ ) is the wind speed (temperature) at the 10-m height,  $T_s$  is the lake surface temperature, and  $C_H$  is the sensible heat exchange

coefficient, which usually changes with season and wind speed, etc. To reduce the influence of  $C_H$ ,  $T_s$  is calculated only when  $H_s$  is close to 0  $\text{W s}^{-1}$  [i.e., the transition of  $H_s$  from positive (negative) to negative (positive)]. At this moment,  $T_s$  is set to  $T_{10}$  because the other coefficients in the right hand side of Eq. (1) cannot equal 0. Although this method can only estimate a few  $T_s$  values in a day, it is enough for the study because of the relatively slow variation (less than 2.5°C) of  $T_s$  within a day (Xu and Ouyang, 1989).

The time series of 30-min mean sensible heat flux and air temperature over PL are shown in Fig. 2. The air temperature rapidly increased from 22.5°C at 0200 UTC [1000 local solar time (LST)] to the peak of 27.2°C at 0800 UTC (1600 LST), and then varied slowly. In contrast, the sensible heat flux rapidly decreased from 8.0  $\text{W m}^{-2}$  at 0300 UTC (1100 LST) to -7.8  $\text{W m}^{-2}$  at 0600 UTC (1400 LST), and then fluctuated with a small amplitude. In the evolution of sensible heat flux, there were four transition points at 0430 UTC (1230 LST; point A), 0900 UTC (1700 LST; point B), 0930 UTC (1730 LST; point C), and 1145 UTC (1945 LST; point D), corresponding to the air temperatures of 25.45, 26.35, 26.45, and 26.43°C, respectively (Fig. 2). These air temperatures approximately represent the lake temperatures at these four times. Due to the solar radiation and heating of

overlying warm air (i.e., negative sensible heat flux), the lake temperature increased by 0.9°C from 0430 UTC (1230 LST; i.e., point A) to 0900 UTC (1700 LST; i.e., point B). After 0800 UTC (1600 LST), the lake temperature remained at approximately 26.4°C. The MODIS MYD11A1 data show that about two days ago (i.e., at 1730 UTC on 11 May 2015), the lake surface temperature of PL was about 23°C. Unfortunately, the MODIS data over PL on 12 and 13 May 2015 were missing. But this is adequate to suggest that the lake temperature calculated by Eq. (1) is credible because the lake is continuously heated by the hot sun in the following two days.

Wind is also an important factor for lake-effect and lake-enhanced events (Carpenter, 1993; Miner and Fritsch, 1997; Laird et al., 2010, 2016; Metz, 2011; Lombardo and Colle, 2012; Workoff et al., 2012). Although several stations collect the 10-m wind around PL (only national basic or reference stations observe the wind), no station is located in PL. In order to reveal the wind over PL clearly, the integrating velocity–azimuth process (IVAP) wind (i.e., the radar retrieved winds) proposed by Liang (2007) is used, because it is smoother than VAP and UW (uniform-wind) wind, and has higher spatial resolution than the velocity–azimuth display (VAD) wind. The calculation of the IVAP wind (Liang, 2007) is as follows,

$$u = \frac{\int_{\beta_1}^{\beta_2} V_\beta \cos \beta d\beta \int_{\beta_1}^{\beta_2} \sin^2 \beta d\beta - \int_{\beta_1}^{\beta_2} V_\beta \sin \beta d\beta \int_{\beta_1}^{\beta_2} \sin \beta \cos \beta d\beta}{\int_{\beta_1}^{\beta_2} \cos^2 \beta d\beta \int_{\beta_1}^{\beta_2} \sin^2 \beta d\beta - (\int_{\beta_1}^{\beta_2} \sin \beta \cos \beta d\beta)^2}, \quad (2)$$

$$v = \frac{\int_{\beta_1}^{\beta_2} V_\beta \sin \beta d\beta \int_{\beta_1}^{\beta_2} \cos^2 \beta d\beta - \int_{\beta_1}^{\beta_2} V_\beta \cos \beta d\beta \int_{\beta_1}^{\beta_2} \sin \beta \cos \beta d\beta}{\int_{\beta_1}^{\beta_2} \cos^2 \beta d\beta \int_{\beta_1}^{\beta_2} \sin^2 \beta d\beta - (\int_{\beta_1}^{\beta_2} \sin \beta \cos \beta d\beta)^2}, \quad (3)$$

where  $V_\beta$  is the observed radial velocity at an azimuth angle of  $\beta$  and a given gate (range). The sector  $[\beta_1, \beta_2]$  is set to 24° in this study.

### 3. Observational analysis

#### 3.1 Evolution of the storm

After the sunset (at about 1100 UTC or 1900 LST) on 13 May 2015, a convective storm with the maximum reflectivity more than 50 dBZ moved eastward to PL from the Mufu Mountains at 1200 UTC (2000 LST), and the echoes with the reflectivity more than 30 dBZ almost completely covered PL (Fig. 3a). The intense echoes (more than 45 dBZ) were mainly located to the southwest of PL, and the echoes over PL did not strengthen (Fig. 3a). At this moment, the area to the west of PL experienced a drastic decrease in air temperature from

about 28°C to about 21°C within 4 h (Figs. 4a, b). This is a joint contribution of the storm-induced cooling (evaporation and cold pool) and the radiation cooling after the sunset. By 1300 UTC, the air temperature in the west of PL also decreased to about 21°C as the storm continued to move eastward (Fig. 4c). The land surface temperature around PL had a similar evolution, but was 1–2°C lower than that of the air temperature (figure omitted). The lake–land temperature difference reached about 6°C (the lake temperature is about 26°C), which favors genesis of the lake–land breeze and lake-effect events (Steenburgh et al., 2000). Although the storm was slightly weakened overall (the area of echoes more than 35 dBZ slightly reduced), the echoes over PL exhibited an enhancement, reaching above 45 dBZ or even 50 dBZ at the east shore, the north shore, and the middle of PL at 1300 UTC (2100 LST) (Fig. 3b).

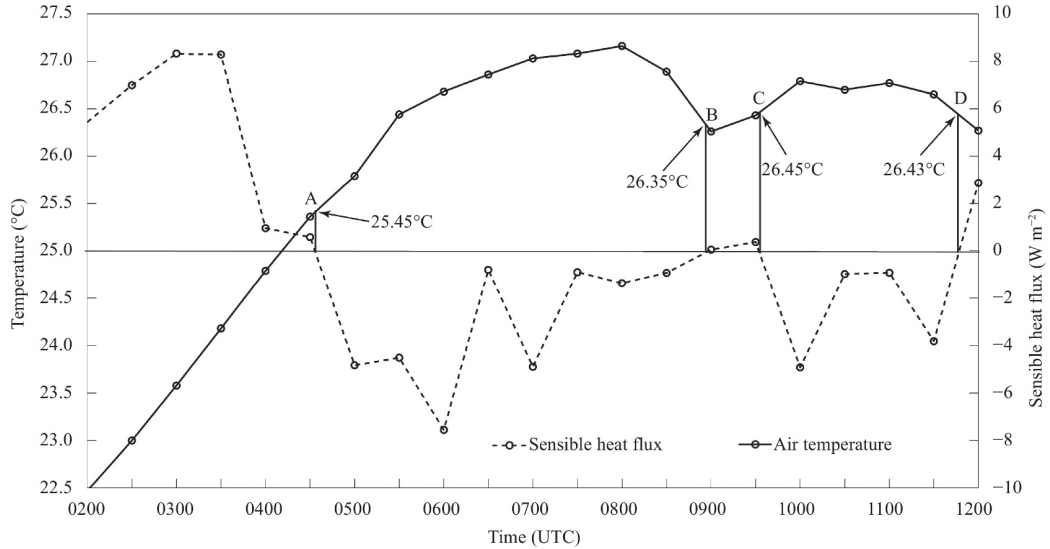


**Fig. 2.** Time series of the air temperature (left-hand axis; solid line) and sensible heat flux (right-hand axis; dashed line) measurements over PL from 0200 to 1200 UTC on 13 May 2015.

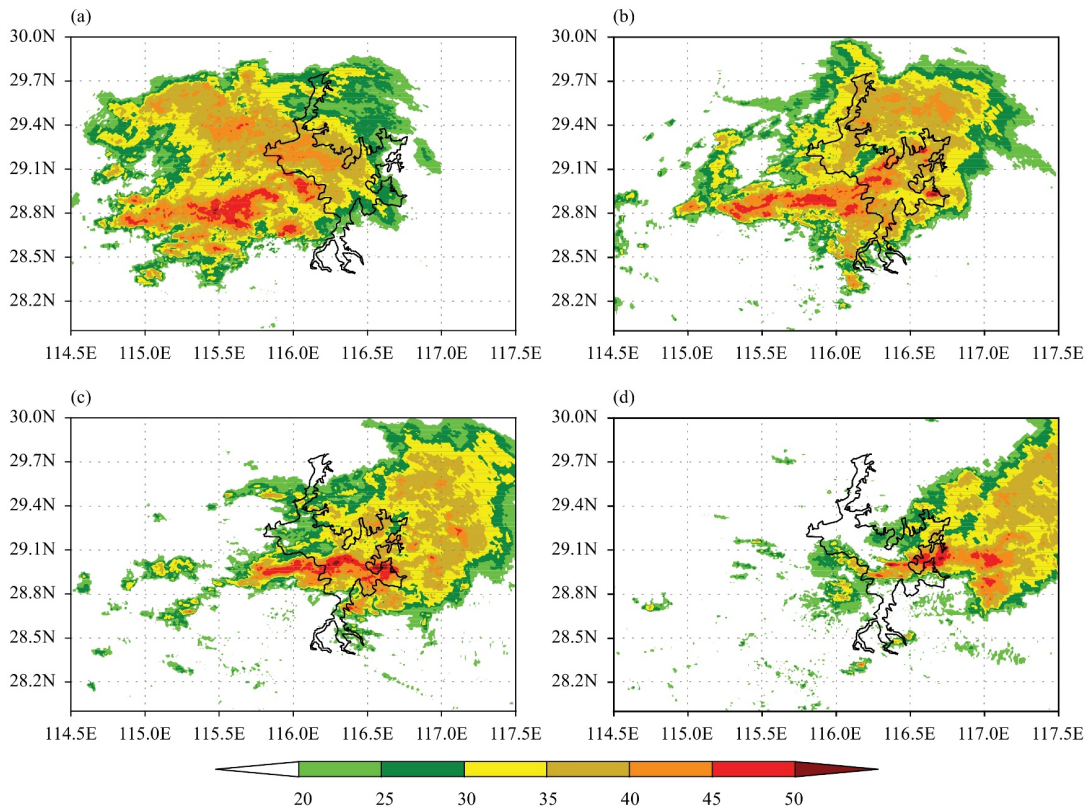


**Fig. 3.** Composite radar reflectivity (shading; dBZ) distributions observed by NANC CINRAD-SA radar at (a) 1200, (b) 1300, (c) 1400, and (d) 1500 UTC on 13 May 2015. The black curve denotes the boundary of PL.

With the storm moving eastward, the air temperature over the whole PL and its adjacent areas decreased to about 21  $^{\circ}\text{C}$  at 1400 UTC (2200 LST) (Fig. 4d). It is noted that the air temperature in the region to the southeast of PL, which was less affected by the storm, was still

more than 24  $^{\circ}\text{C}$  (Figs. 3, 4d). At this moment, the area of echoes more than 35 dBZ was further decreased compared to that at 1300 UTC (2100 LST), indicating that the storm was still weakening. However, more importantly, the echoes over PL and its downwind side were

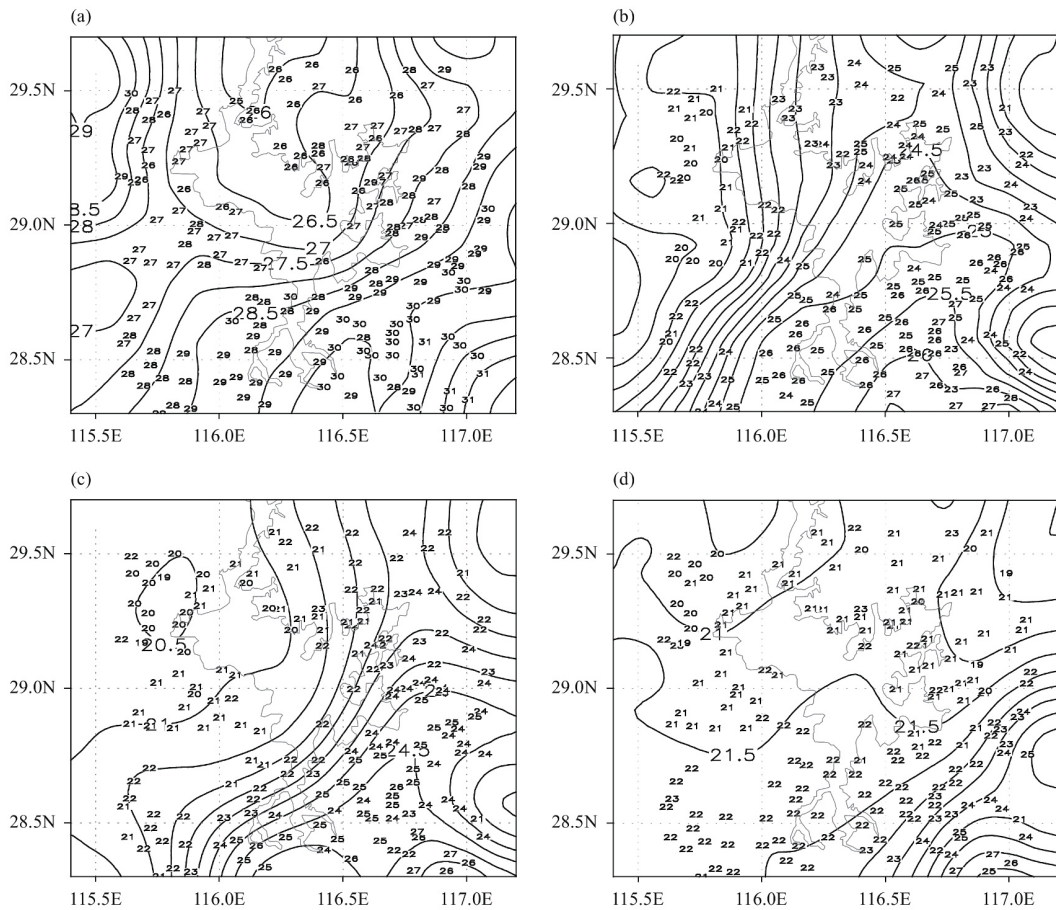


**Fig. 4.** Distributions of 2-m air temperature (contour; °C) around PL at (a) 0800, (b) 1200, (c) 1300, and (d) 1400 UTC on 13 May 2015.

obviously strengthened (the area with the echo more than 45 or 50 dBZ was enlarged), forming an intense east–west banded echo (Fig. 3c). Then the storm continued to move eastward, with the main body moving away from PL at 1500 UTC (2300 LST). Nevertheless, the intense east–west banded echo remained over PL and its downwind side, with the maximum reflectivity of above 50 dBZ (Fig. 3d). Finally, the echoes over PL and the downwind side disappeared at 1630 UTC 13 May (0030 LST 14 May; figure omitted). It can be seen from the evolution of the storm crossing PL that although the storm is weakened overall, the echoes over PL and its downwind side are enhanced. Apparently, this event is a lake-enhanced convection event.

Figure 3 shows the enhancement of echoes over PL and its downwind side when the storm crossed it. As can be seen, the enhancement is not quite significant. The overall weakening and the large size (compared with PL) of the storm may be responsible for this. In order to display the change of the storm crossing PL more clearly, a Hovmöller's diagram of the averaged reflectivity between  $28.8^\circ$  and  $29.2^\circ\text{N}$  (this range covers the main

body of PL) is plotted in Fig. 5a. It is shown that the echoes significantly strengthened over PL and its downwind side after 1300 UTC (2100 LST) on 13 May 2015, with the reflectivity increasing to above 44 dBZ from about 40 dBZ (Fig. 5a). Moreover, the duration of the intense echoes (above 34 dBZ) over PL was obviously prolonged, with the duration extended for about 1 h over PL and its downside (Fig. 5a). This prolongation is probably also related to the lake effect (Laird et al., 2009; Alcott et al., 2012). The frequency image of reflectivity above 25 dBZ from 1200 UTC 13 May (2000 LST 13 May) to 1700 UTC 13 May (0100 LST 14 May), which is developed by Slemmer (1998) and then used by Steenburgh et al. (2000) to identify the lake-effect precipitation over the Great Salt Lake, is drawn in Fig. 5b (with a total of 50 radar scans). This period covers the whole process of the storm crossing over PL. Figure 5b shows that the frequencies above 0.6 are arranged in several zonal belts, which respectively located over PL and its downwind side, as well as the north shore. The frequencies above 0.7 are also organized in a zonal belt situated to the east of PL (i.e., the downwind side; Fig. 5b). It is

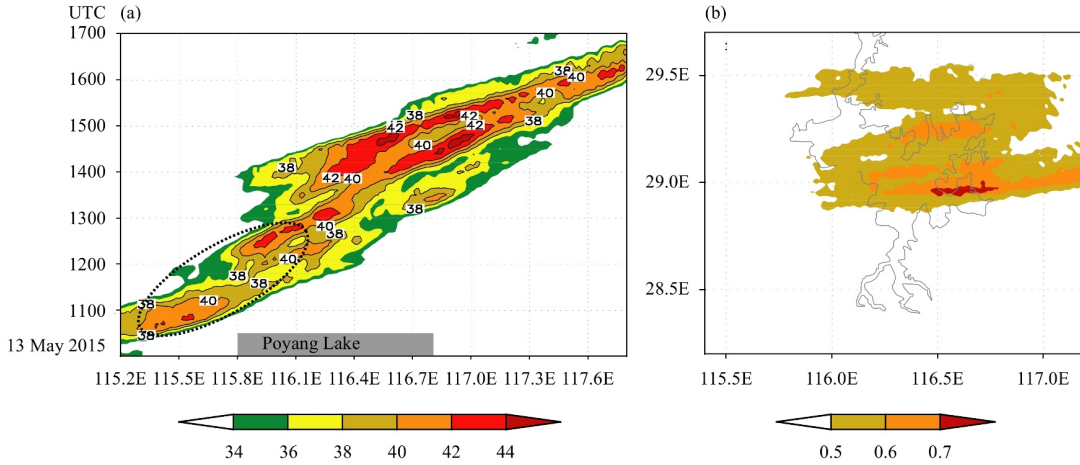


**Fig. 5.** (a) Hovmöller diagram of reflectivity (dBZ) averaged between 28.8° and 29.2°N and (b) the frequency image of reflectivity above 25 dBZ from 1200 to 1700 UTC on 13 May 2015. The enhancement in the dotted ellipse in (a) may be induced by the complex topography.

clear that both the Hovmöller's diagram and the frequency image confirm that the storm is a lake-enhanced storm.

It is noted that the echoes to the west of PL were persistently stronger than those to the north of PL during the period of 1200–1500 UTC (2000–2300 LST) (Figs. 3a–c). Figure 5a also shows that the echoes to the west of PL had an enhancement before 1300 UTC (2100 LST) (i.e., the area encircled by the dotted ellipse). As seen from Fig. 1b, the topography to the southwest of PL is quite complex. A southwest–northeast “narrow pipe” resides between the Mufu Mountains and an isolated mountain to the northwest of NANC. This “narrow pipe” can accelerate the southwesterly or westerly winds. Meanwhile, the blocking of hills near YX and the urban region (e.g.

buildings) of YX is conducive to uplifting of the low-level flows (Wang et al., 2017). Therefore, the enhancement of echoes to the west of PL may be resulted from the complex topography, and further investigation (e.g., with numerical experiments) is needed but beyond the current study. Here, we will focus on the lake-enhanced convective storm in the subsequent section.

### 3.2 The large-scale background

At 1200 UTC (2000 LST) on 13 May 2015 (approaching the onset of the lake-enhanced event), a 500-hPa trough was situated over Southwest China, with the trough axis (dashed line) extending from the southeastern Tibetan Plateau to the northwestern Indochina Peninsula (Fig. 6a). The west-extending ridge point of the

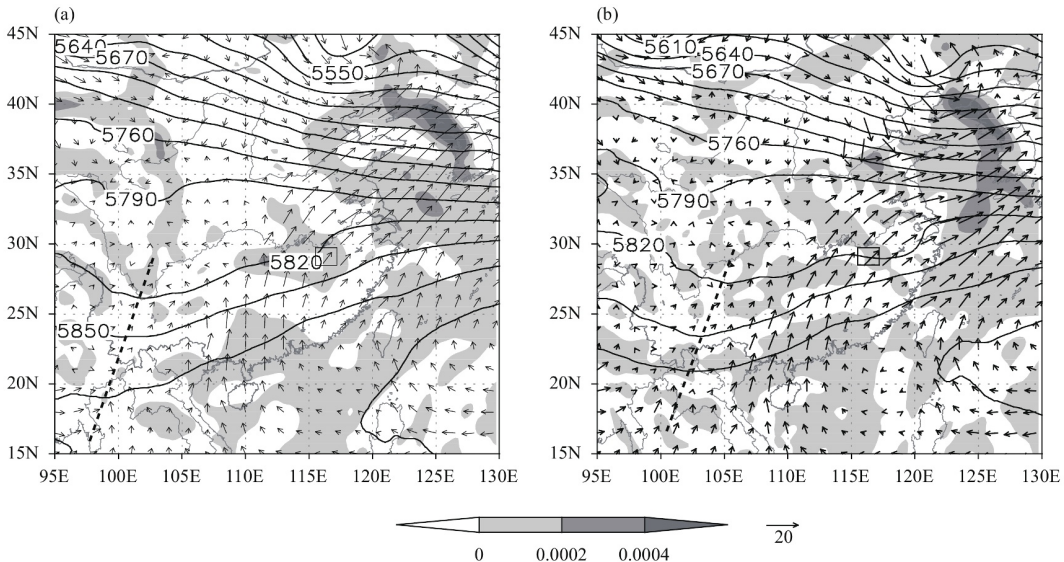


**Fig. 6.** 500-hPa geopotential height (solid line; gpm), 925-hPa wind vector ( $\text{m s}^{-1}$ ), and 925-hPa temperature advection (shading;  $\text{K s}^{-1}$ ) at (a) 1200 and (b) 1800 UTC on 13 May 2015. The dashed line indicates the trough, and the rectangle represents the PL region.

West Pacific subtropical high (WPSH) at 5970 gpm was located near (17°N, 119°E). At 925 hPa, PL (rectangle) was controlled by the southwesterly wind jet ahead of the 500-hPa trough with weak warm advection (a similar pattern at 850 hPa; Fig. 6a), and the low-level jet may play an important role in the development of the convective storm in Fig. 3a through transporting moisture and providing convergence (Du and Chen, 2019). By 1800 UTC 13 May (0200 LST 14 May), approximately 2 h after the end of the lake-enhanced event, the long wave system in the mid-low latitude moved eastward for approximately 300 km, and PL was still controlled by the southwesterly wind and weak temperature advection ahead of the 500-hPa trough (Fig. 6b). The large-scale background with the weak warm advection at low levels is different from those of the typical lake-effect events occurring over the Great Salt Lake and the Great Lakes in North America in the winter season, where the lake-effect events usually occur in the low-level cold advection behind a 500-hPa trough (Carpenter, 1993; Miner and Fritsch, 1997). Lakes in North America can maintain a relative high (low) temperature in the winter (summer) season due to a deep depth and a large coverage or a high salinity (Steenburgh et al., 2000; Kristovich and Spinar, 2005). Moreover, since these lakes locate in high latitudes, they are often intruded by the intense low-level cold advection in the winter season. Therefore, the lake-effect and lake-enhanced events in North America frequently occur in the winter season, especially in the intense low-level cold advection region behind a 500-hPa trough. On the contrary, PL is very shallow, with a mean depth less than 6 m and locates in low latitudes, so it is a heat source at nighttime in the summer season (Wan et al., 1994). Besides, Payer et al. (2007) revealed that a lake-effect snowband over Lake Champlain at 18 January 2003 occurred also in the low-level weak warm advection associated with a warm front (the lake temperature is still higher than the surrounding land temperature).

In fact, the key factor of lake-effect or lake-enhanced event is the lake-air or lake-land temperature difference. If a lake is obviously warmer than the overlying air (or the surrounding land surface), the lake-effect and lake-enhanced events are probable to develop. Steenburgh et al. (2000) indicates that a large (usually more than 6°C) land-lake temperature difference is favorable for land breezes developing, which can make the overlying air converge to the lake center. Carpenter (1993), Steenburgh et al. (2000) and Laird et al. (2009) have suggested that the temperature lapse rate below 700 hPa favorable to develop lake-effect and lake-enhanced events should be larger than the dry-adiabatic lapse rate.

However, Parcel theory suggests that any lapse rate larger than the moist-adiabatic lapse rate could be sufficient for the airflow over the lake to yield a buoyant surface parcel, when the atmosphere is saturated (Alcott et al., 2012). For the lake-effect event over the Great Salt Lake at 1200 UTC on 2 January 2000, under the near-saturation ambient condition, the lapse rate was only approximate moist-adiabatic lapse rate (Alcott et al., 2012). Figure 7a shows the sounding profile at NANC at 1200 UTC (2000 LST). The air temperature profile from 925 to 700 hPa was situated between the moist-adiabatic line and the dry-adiabatic line. The temperature-dewpoint spread below 700 hPa was about 5°C, with the minimum of about 3°C at 850 hPa and near surface, indicating a relatively moist ambient condition. Besides, the convective available potential energy (CAPE) was 54 J, and the lifting condensation level (LCL) is only about 700 m (below 950 hPa). The profile of pseudo-equivalent potential temperature ( $\theta_{se}$ ) at NANC shows that there was a significant convectively unstable layer ( $\partial\theta_{se}/\partial p > 0$ ) between 850 and 700 hPa, and a stable layer ( $\partial\theta_{se}/\partial p < 0$ ) between 925 and 850 hPa (this was induced by the low dewpoint temperature at 925 hPa), which can suppress the upward transport of warm and moist air near the surface (Fig. 7b).

### 3.3 The heating and moistening by PL

The  $T$ -log  $P$  diagram in Fig. 7a shows profiles of the atmospheric thermodynamic variables over NANC. The profiles over PL may be different due to the lake's heating and moistening, which are realized by sensible and latent heat fluxes. Assuming a linear vertical profile of the sensible heat flux, the amount of heating by a lake for its overlying air in the temporal mean depth ( $\bar{z}_i$ ) of the mixed layer over the time period of  $\Delta t$  (i.e., the time that air takes to travel across the lake) can be expressed (Markowski and Richardson, 2010) as,

$$\Delta\theta_a \approx \frac{1.2c_h L \overline{(\theta_0 - \theta_a)}}{\bar{z}_i}, \quad (4)$$

where  $c_h = 0.002$  is a bulk transfer coefficient for heating,  $L$  is the distance traveled over a lake surface, and  $\theta_0$  ( $\theta_a$ ) is the lake (2-m air) potential temperature. Since the low-level flows are westerly winds (Fig. 7a),  $L$  is set to 75 km based on the east-west length of PL. The lake temperature is about 26.4°C (Fig. 2) and the 2-m air temperature is about 21°C (Fig. 4d), resulting in  $\overline{(\theta_0 - \theta_a)} \approx 5^\circ\text{C}$ . Besides, the mean depth  $\bar{z}_i$  of mixed layer during this event is about 750 m based on the ERA-interim data (i.e., the mean boundary layer height). Therefore, Eq. (4) yields  $\Delta\theta_a \approx 1.2^\circ\text{C}$ . This indicates that PL can increase the air

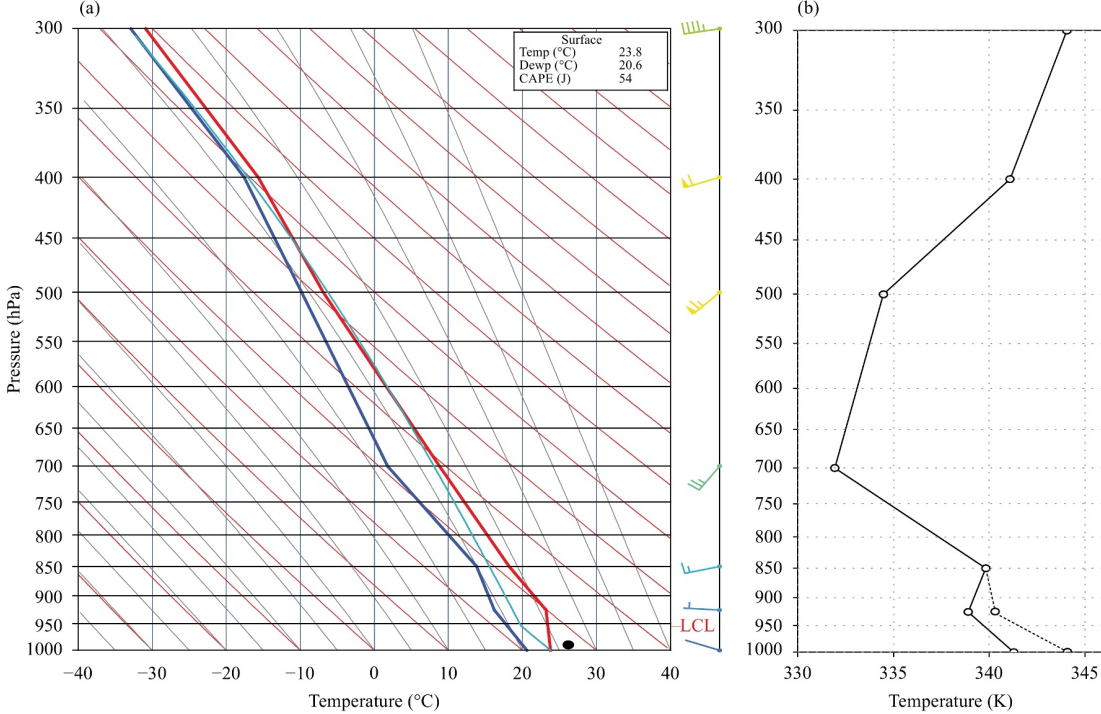


**Fig. 7.** Sounding observations at NANC at 1200 UTC 13 May 2015. (a)  $T$ -log $P$  diagram, in which the temperature (dewpoint) profile is denoted by the red (blue) heavy line; the temperature of an air parcel lifted from the surface is denoted by the light blue line; the solid circle represents the lake temperature of PL; and full and half wind barbs denote 4 and 2 m s<sup>-1</sup>, respectively. (b) The profile of pseudo-equivalent potential temperature ( $\theta_{se}$ ) at NANC at 1200 UTC. The dashed line represents the modified  $\theta_{se}$  by PL.

potential temperature in the mixed layer by about 1.2°C.

Similarly, supposing that the vertical profile of the water vapor flux is also linear, the amount of moistening by a lake for the overlying air over the period  $\Delta t$  is calculated as follows (Markowski and Richardson, 2010),

$$\Delta r_{va} \approx \frac{0.4c_e L(\bar{r}_{v0} - \bar{r}_{va})}{\bar{z}_i}, \quad (5)$$

where  $c_e = 0.002$  is the bulk transfer coefficient for moistening, and  $r_{v0}$  ( $r_{va}$ ) is the saturation water vapor mixing ratio at the lake surface (2-m height). In the current case, the lake surface temperature of 26.4°C corresponds to  $r_{v0} \approx 21$  g kg<sup>-1</sup>, and the dewpoint temperature of 20.6°C at NANC (Fig. 7) is consistent with  $r_{va} \approx 15$  g kg<sup>-1</sup>. Therefore,  $(\bar{r}_{v0} - \bar{r}_{va}) \approx 6$  g kg<sup>-1</sup>, and Eq. (5) yields  $\Delta r_{va} \approx 0.48$  g kg<sup>-1</sup>, implying moistening of about 0.48 g kg<sup>-1</sup> by PL on overlying air (it is equivalent to an about 0.5°C increment for the dewpoint temperature). Due to the heating and moistening of PL, the low-level (925 and 1000 hPa)  $\theta_{se}$  over PL is increased, with an approximate correction shown in Fig. 7b (dashed line). More importantly, the stable layer located between 925 and 850 hPa disappears as the 925-hPa  $\theta_{se}$  increases, and the CAPE also increases to about 280 J. This indicates that the heating and moistening of PL can destabilize the ambient

stable layer between 925 and 850 hPa, in favor of the upward transport of near-surface warm and moist air.

### 3.4 Winds

The IVAP wind at 1-km height over PL, which is calculated by Eqs. (2) and (3) based on the radial velocity of NANC radar, indicates that there is significant convergence with westerly and southwesterly winds along the northeast–southwest axis of PL (Fig. 8a). In contrast, the wind outside of PL has no obvious convergence (Fig. 8a). The longitude–height cross-section of reflectivity and IVAP wind (averaged between 28.8° and 29.1°N) at 1345 UTC (2145 LST) exhibits intense convergence (dashed rectangle) at low levels (below 4 km) and strong divergence (solid-line rectangle) at high levels (above 7.5 km) over PL (Fig. 8b), and the strong echoes are just located in the region with the strong low-level convergence and high-level divergence (i.e., in the middle and east of PL; Fig. 8b). Moreover, the Hovmöller diagrams of divergence at 2 km (here, the divergence at 1 km is not used because the 1-km IVAP wind has more missing values due to the effect of radar elevation and the earth curvature) and 8 km show that the low-level convergence was enhanced over PL from 1300 UTC 13 May (2100 LST 13 May) to 1600 UTC 13 May (0000 LST 14

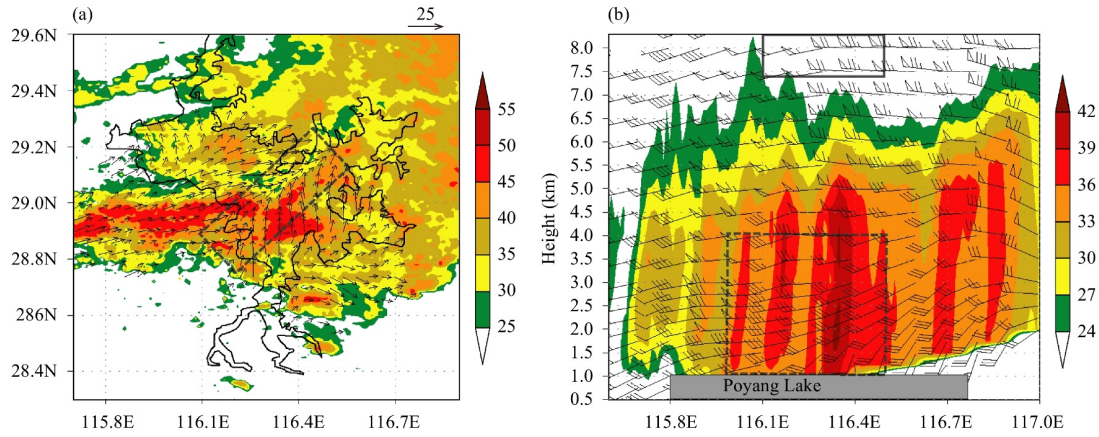


**Fig. 8.** (a) The distribution of composite reflectivity (dBZ) and IVAP wind ( $\text{m s}^{-1}$ ) at 1-km height and (b) the cross-section of reflectivity (dBZ) and IVAP wind averaged between  $28.8^\circ$  and  $29.1^\circ\text{N}$  at 1345 UTC (2145 LST) on 13 May 2015. Dashed rectangles represent the region with strong convergence, while the solid-line rectangle indicates the area of divergence.

May) (Fig. 9a), while the high-level divergence was also enhanced over PL and on its downwind side (Fig. 9b). Apparently, the evolutions of IVAP wind and its divergence (Figs. 8, 9) imply that the wind over PL is beneficial to the enhancement of the storm crossing PL.

It is noted that the low-level IVAP wind with convergence of westerly wind and southwesterly wind is jointly induced by the ambient wind, convection induced wind, and the large land–lake temperature difference induced land–lake breeze. Although it is difficult to separate them, it is not necessary to do so since the evolution of the crossing storm is influenced together by all the winds. In fact, the low-level converged wind over PL (Fig. 8a) is favorable for lifting the moistened and heated air to above the LCL, facilitating the condensation, and releasing the latent heat. In turn, the released latent heat

is conducive to warming the surrounding air, increasing the upward motion, and finally enhancing the crossing storm. Besides, the high-level outflow of the crossing storm is also strengthened as the crossing storm strengthens. This is responsible for the enhanced divergence of IVAP wind at 8 km over PL and on its downwind side (Fig. 9b).

#### 4. The WRF model simulation

The above observational analysis shows that the convective storm was strengthened when it passed through PL during 1300–1600 UTC on 13 May 2015, and the heating and moistening of PL may be responsible for the enhancement of the storm under the convectively unstable and relatively moist condition. In order to confirm

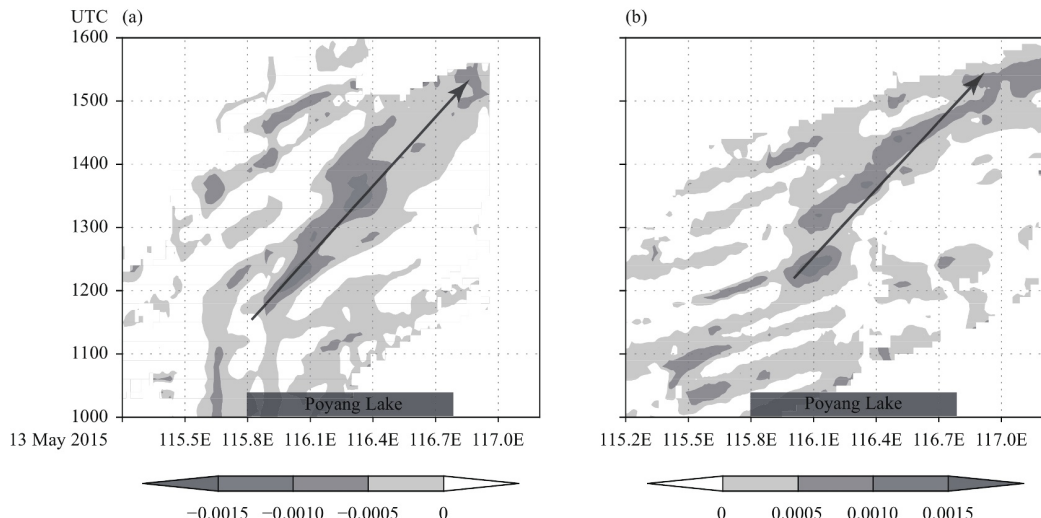


**Fig. 9.** Hovmöller diagram of divergence (shading;  $\text{s}^{-1}$ ) of IVAP wind averaged between  $28.8^\circ$  and  $29.1^\circ\text{N}$  at (a) 2 and (b) 8 km. The arrows indicate the propagation direction of convergence or divergence.

the impacts of PL on the atmospheric thermodynamics and the crossing storm, and to clarify the relationship between the heating and moistening of PL and the low-level convergence, numerical simulations using the WRF model and corresponding diagnostic analysis are performed and results are presented next.

#### 4.1 Model description and experiment design

The WRF model V3.9 released in April 2017 is used for this study. The numerical simulations include a control experiment (CTR) and a sensitivity experiment (SES). In the CTR, there are three one-way nested domains (d01, d02, and d03) with the largest one d01 centered at (29.1°N, 116.3°E) and the smallest one d03 shown in Fig. 1b. Their horizontal resolutions are 15, 5, and 1.67 km, respectively. The model's top is set at 50 hPa. The cumulus convection is parameterized with the Grell–Freitas scheme (Grell and Freitas, 2014), because it has a good performance in South China (Wu et al., 2018). No cumulus parameterization schemes are used in d02 and d03. The microphysics schemes in the three domains are the Thompson scheme, which has the advantage in simulating the lake-effect precipitation (McMillen and Steenburgh, 2015). Land surface, planetary boundary layer, and longwave radiation are 5-layer thermal dif-

fusion scheme, Yonsei University scheme, and the Rapid Radiative Transfer Model (RRTM) scheme, respectively. The model is forced with lateral and initial conditions from the NCEP final (FNL) operational model global tropospheric analysis data with 6-h temporal and  $1^\circ \times 1^\circ$  spatial resolutions. Moreover, the sounding data in East Asia at 1200 UTC 12 May 2015 are assimilated to improve the initial condition by using the WRF three-dimensional variational (3DVAR) system. The lake surface temperature of PL in the model is also modified to 26.4°C at the initial time (1200 UTC 12 May 2015). The model integrates with a time step of 45 s for 28 h until 1600 UTC. In SES, the setting is the same as that in CTR, except that the water body of PL is substituted by arable land (AL).

#### 4.2 CTR experiment

Firstly, the simulated radar reflectivity in CTR is validated against the observation. The simulated storm with the maximum reflectivity more than 25 dBZ traveled across PL from southwest to northeast before 1200 UTC (figure omitted). In about half an hour, the tail of the storm showed enhancement and its maximum reflectivity exceeded 25 dBZ (Fig. 10a). Then, the tail of the storm continued to strengthen, widen, and move north-

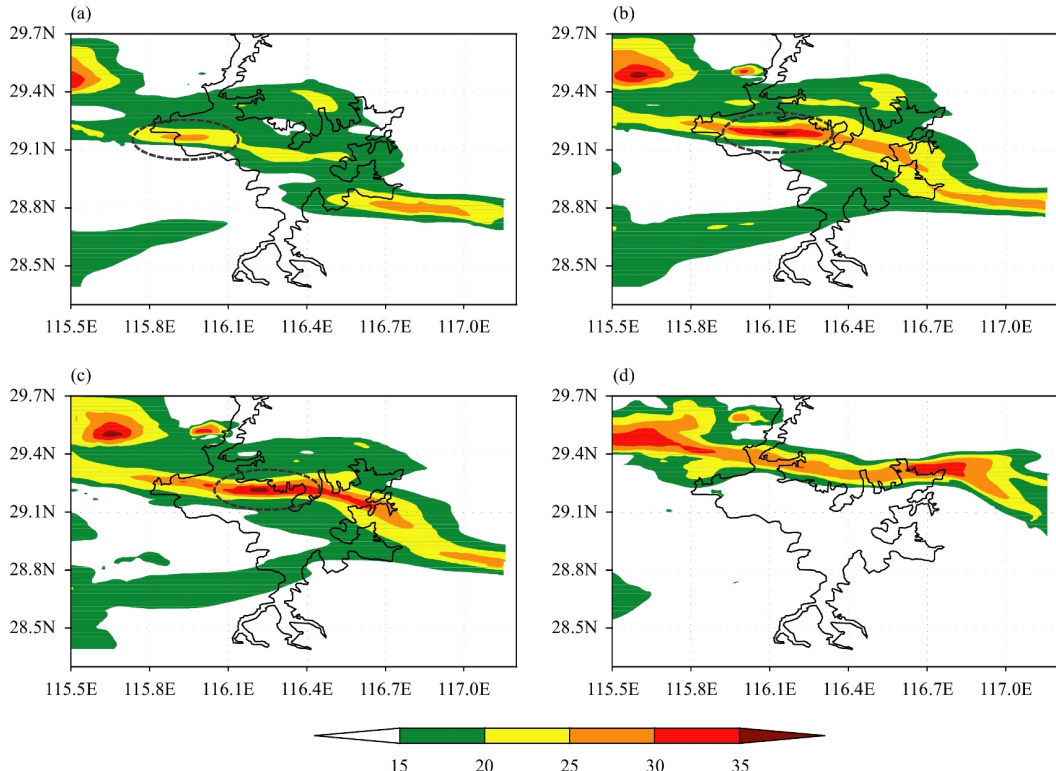


**Fig. 10.** The maximum reflectivity (shading; dBZ) in domain d03 in CTR at (a) 1230, (b) 1430, (c) 1500, and (d) 1600 UTC on 13 May 2015. The dashed ellipse in (a)–(c) represents the region in which the echoes are significantly enhanced.

eastward. At 1430 UTC (i.e., 2 h later), the intense echoes (larger than 25 dBZ) developed into a zonal belt that stretched over PL (Fig. 10b), with the maximum reflectivity of above 35 dBZ. By 1500 UTC, the intense echo belt was close to the mid–north shoreline of PL, with the coverage enlarged for the echoes above 30 dBZ (Fig. 10c). Subsequently, the intense echo belt kept on moving northeastward, and it moved out of PL from the northern shoreline at 1600 UTC, with the maximum reflectivity decreased to below 35 dBZ (Fig. 10d). Two hours later, the storm around PL vanished. CTR shows that after the spearhead of the storm swept over PL, the tail of the storm exhibited a distinct enhancement over PL and on its downwind side, especially for the region encircled by a dashed ellipse in Fig. 10. Although there are small differences in the intensity and movement of the storm between the simulation and observation, CTR has successfully reproduced the evolution of the storm crossing PL during 1200–1600 UTC on 13 May 2015.

The Hovmöller diagram of the maximum reflectivity, sensible heat flux, and latent heat flux in CTR is given in Fig. 11a. It is clear that the simulated storm started to significantly strengthen over PL and on its downwind side after 1330 UTC. This coincides with the observations depicted in Figs. 3, 5a, and further verifies the performance of CTR. In addition, at about 1300 UTC (2100 LST), the sensible heat flux over PL (the central–eastern PL) turned positive from the previous negative value, and the latent heat flux increased from about 150 W m<sup>-2</sup> to approximately 200 W m<sup>-2</sup> (Fig. 11a). This indicates that at this moment, the heat content in PL began to transfer into the overlying air, and the water vapor transport from PL into the air also remarkably increased.

At 1200 UTC 13 May 2015, the 850-hPa high-humidity area (relative humidity more than 75%) ahead of the 500-hPa trough (Fig. 6a) was located south of the Yangtze River and west of 117.5°E, with the maximum center (relative humidity more than 90%) in the middle of South China (Fig. 12a). Moreover, PL was situated in the northeast of the high-humidity area, with strong moisture advection. At this moment, the lake-effect boundary layer (LBL) in CTR appeared over PL (Fig. 12b). LBL was identified by the largest positive vertical gradient of  $\theta_{se}$ , and produced by the heating and moistening of the lake (Barthold and Kristovich, 2011; Owens et al., 2017). On the east shore of PL, the LBL approached 900 hPa (about 1 km). It can also be seen from Fig. 12b that the near-surface (925 hPa)  $\theta_{se}$  over PL was about 5 (2) K larger than that on the upwind side of PL, which was similar to the estimation of the heating and moistening of PL (see Section 3.3). Meanwhile, a high  $\theta_{se}$  tongue with the center at about 850 hPa extended over PL from the west, with an obvious convectively unstable layer ( $\partial\theta_{se}/\partial p > 0$ ) between 850 and 700 hPa and a convectively stable layer under 850 hPa (Fig. 12b). This convectively unstable layer corresponded to the storm moving eastward in Figs. 3a, 11a. Then, the high  $\theta_{se}$  tongue strengthened and moved eastward and downward. By 1500 UTC (i.e., the time when the simulated storm over PL significantly strengthened), the center of the high  $\theta_{se}$  tongue fell to about 900 hPa (this is in fact induced by the obvious increase of the meridional wind at this level), with the maximum of above 348 K. The high  $\theta_{se}$  tongue and the PL-induced LBL merged into a deep (surface–700 hPa) unstable layer over PL (Fig. 12c). Apparently, the heating and moistening of PL on overlying air have

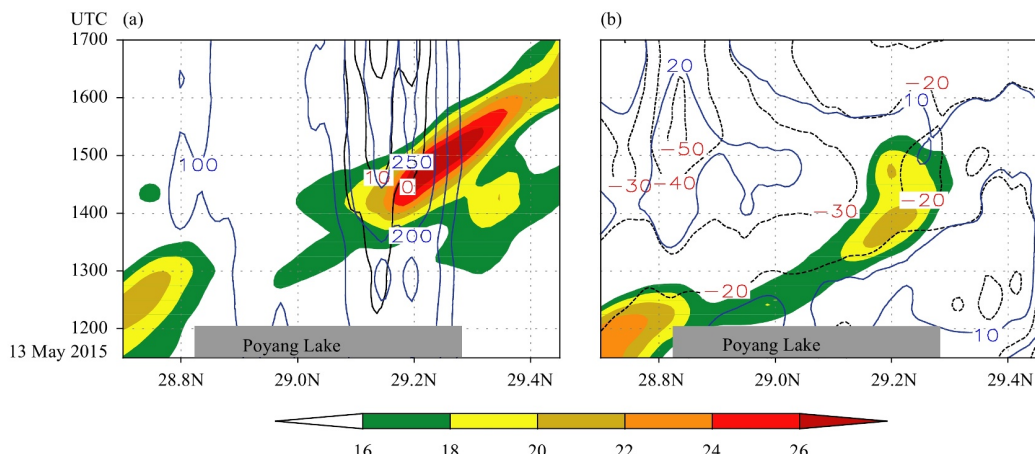


**Fig. 11.** Hovmöller diagrams of simulated maximum reflectivity (shading; dBZ), sensible heat flux (black line; W m<sup>-2</sup>), and latent heat flux (blue line; W m<sup>-2</sup>) averaged between 115.85° and 116.7°E in (a) CTR and (b) SES. The blue numbers are labeled for blue lines, while the red numbers are marked for black lines.

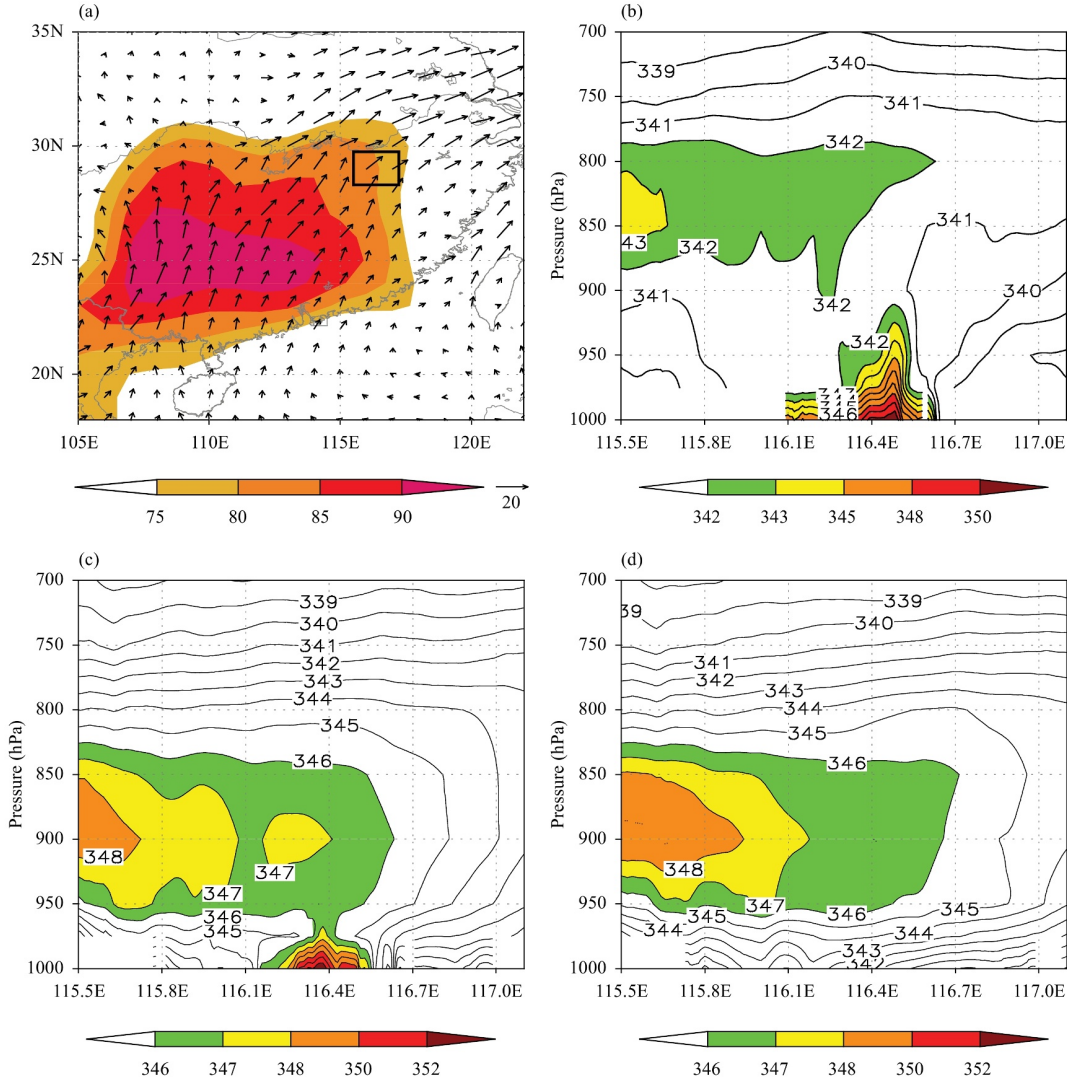


**Fig. 12.** (a) The 850-hPa wind (vector;  $m s^{-1}$ ) and relative humidity (shading; %) fields, (b) the cross-section (along  $29.1^{\circ}N$ ) of  $\theta_{se}$  (K) in CTR at 1200 UTC, and the cross-section of the simulated  $\theta_{se}$  (K) in (c) CTR and (d) SES at 1500 UTC 13 May 2015. The solid-line rectangle represents the PL region.

produced a LBL, which destabilized the ambient stable layer under 850 hPa, opening the upward transporting passage for the near-surface warm and moist air over PL.

#### 4.3 SES experiment

In order to verify the effect of PL on the crossing storm, the water body of PL is replaced with AL in SES. Similar to CTR, a storm with the maximum reflectivity more than 30 dBZ passed through PL (modified with AL) from the southwest to northeast at 1230 UTC 13 May 2015 (Fig. 13a), and then the tail of storm slightly weakened over the modified PL at 1310 UTC (Fig. 13b). When the tail of the storm moved to the north shore of PL, it started to strengthen (Figs. 13c, d). In fact, the enhancement mainly resulted from the surface inhomogeneity due to the hills to the north of PL and the flat AL in

PL (figure omitted). Importantly, in the whole process of the storm crossing PL, its maximum reflectivity (which is less than 35 dBZ; Fig. 13) is obviously smaller than that of CTR (which is more than 35 dBZ) (Fig. 10). Besides, the Hovmöller diagram of simulated maximum reflectivity in SES depicts the evolution of the storm (Fig. 11b). There was no echo with the reflectivity above 16 dBZ in south of the north shore of PL (i.e., south of about  $29.15^{\circ}N$ ) after 1400 UTC, which was quite different from the observation (Fig. 5a) and the CTR (Fig. 11a). Especially, the maximum reflectivity over PL and on its downwind side in SES is approximately 6 dBZ smaller than that in CTR (Fig. 11), which is in accordance with the increment of observational echoes when the storm passes through PL (Fig. 5a). These indicate that the presence of PL with the water body authentically strengthens

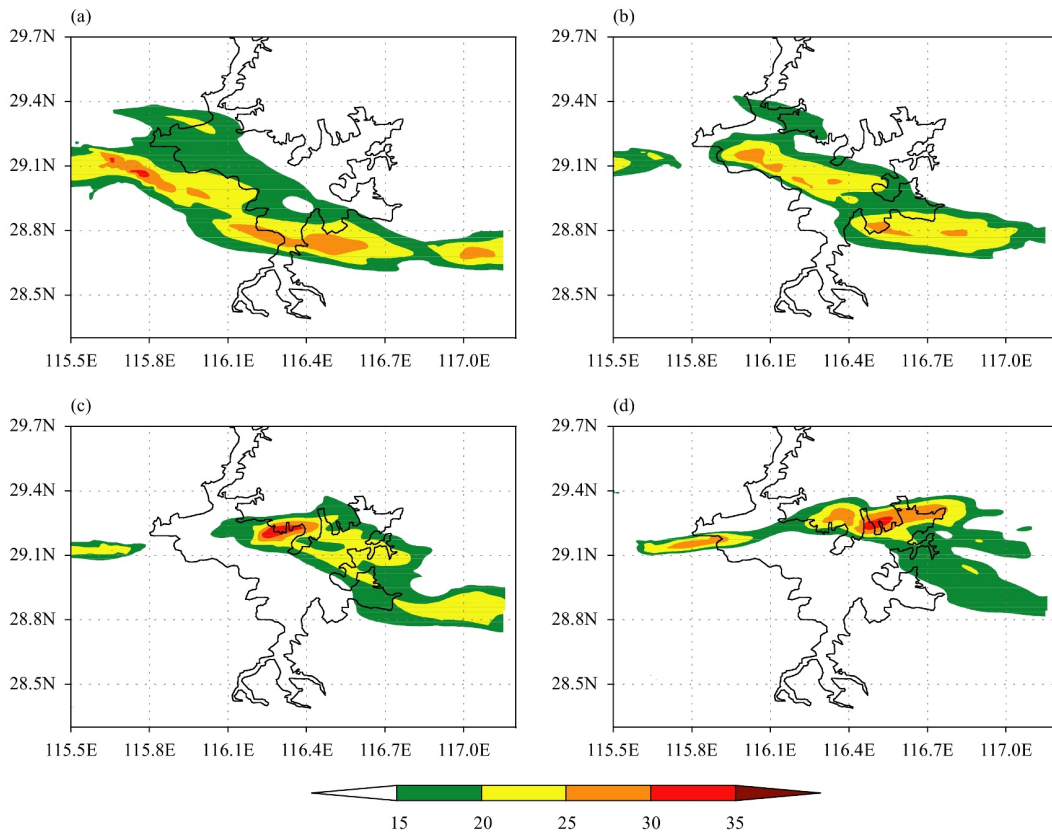


**Fig. 13.** The maximum reflectivity (shading; dBZ) in domain d03 in SES at (a) 1230, (b) 1310, (c) 1400, and (d) 1440 UTC on 13 May 2015.

the crossing storm.

It is significantly different from CTR that the sensible heat flux and latent heat flux over PL in SES do not exhibit an obvious enhancement when the storm is crossing over PL (Fig. 11b). The sensible heat flux over PL is negative with the value of about  $-30 \text{ W m}^{-2}$  in the whole process, while the latent heat flux is 10 times smaller than that of CTR, with the value of about  $15 \text{ W m}^{-2}$ . This indicates that after the water body of PL is replaced by AL, PL could absorb (rather than emit) heat from the overlying air and transport a small amount of water vapor into the overlying air. Therefore, the LBL is not produced in SES, and the stable layer below 900 hPa still maintains (Fig. 12d).

To examine the impact of PL on the low-level wind, the difference of 900-hPa wind between CTR and SES is plotted in Fig. 14a. It is shown that a cyclone is situated in the northwest of PL and the southerly wind dominates the central and south of PL at 900 hPa. The southwest-easterly wind in the southeast of the cyclone and the southerly wind converge in the northwest of PL, forming a significantly convergent area (the dashed rectangle) at 1430 UTC (Fig. 14a). The convergent region is consistent with the area in which the simulated reflectivity in CTR is re-

markably enhanced (Fig. 10b). It is noted that the low-level obvious convergence over PL is not only presented at 1430 UTC, but also exists within 2 h before the convection arrives at PL (figure omitted). In fact, the convergence (it is in fact the convergence anomaly) over PL reflects the land–lake breeze. The land–lake breeze and the deep unstable layer under 700 hPa (Fig. 12c) have increased the upward motion over PL and on its downwind side (Fig. 14b), finally strengthening the crossing storm. In addition, the water vapor mixing ratio difference (CTR – SES) at the low level is gradually increased with latitude, indicating the moistening of PL (Fig. 14b). However, the water vapor mixing ratio difference (CTR – SES) over PL is negative from 950 to 750 hPa (Fig. 14b), since more water vapor is carried into the high levels by the stronger upward motion and condensation in CTR.

## 5. Conclusions

The CINRAD-SA radar data at NANC (about 50 km southwest of PL) illustrate that the convective storm, which crossed over PL from 1200 to 1600 UTC on 13 May 2015, strengthened over PL and its downwind side

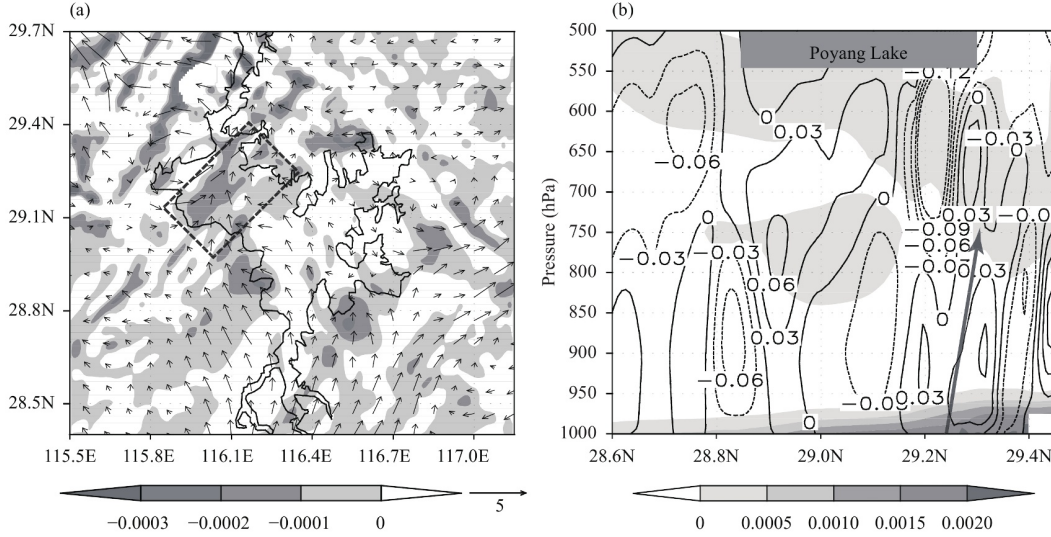


**Fig. 14.** (a) Horizontal distribution of differences in wind (arrow;  $\text{m s}^{-1}$ ) and convergence (shading;  $\text{s}^{-1}$ ) between CTR and SES at 900 hPa, and (b) cross-section of differences in water vapor mixing ratio (shading;  $\text{kg kg}^{-1}$ ) and vertical velocity (contour;  $\text{m s}^{-1}$ ) averaged between  $115.95^{\circ}$  and  $116.4^{\circ}\text{E}$  between CTR and SES, at 1430 UTC on 13 May 2015. The dashed rectangle in (a) represents the region with obvious convergence, and the arrow in (b) indicates the upward motion.

after its spearhead passed through PL. Apparently, this is a lake-enhanced convective storm. Analysis of the large-scale circulation and sounding data shows that the lake-enhanced convection occurred ahead of the 500-hPa trough, with weak low-level temperature advection, a convectively stable layer between 925 and 850 hPa (the layer between 850 and 700 hPa was convectively unstable), and relatively moist ambient air under 700 hPa. This large-scale circulation is different from the typical lake-effect events in North America that usually occur behind the 500-hPa trough with intense cold advection at low levels (Carpenter, 1993; Miner and Fritsch, 1997).

How does this lake-enhanced event form? Due to the heating and moistening of PL on the overlying air, the convectively stable layer between 925 and 850 hPa over PL is destabilized; and instead, a deep (surface–700 hPa) convectively unstable layer is formed. On the other hand, the IVAP wind shows that there is significant low-level (1 km) convergence with westerly and southwesterly wind over PL. The land–lake breeze contributes to the low-level convergence over PL (the ambient winds and convection-induced wind also have contributions), and it is driven by the large (about  $6^{\circ}\text{C}$ ) lake–land temperature difference (Steenburgh et al., 2000) caused by a rapid decrease in the land and air temperature (due to the radiative cooling and storm-induced cooling) after the spearhead of the storm swept over PL. Finally, the deep convectively unstable layer (strengthening the ascending of low-level warm and moist air) and the land–lake breeze (enhancing the convergence of low-level warm and moist

air over PL) over PL jointly strengthen the crossing storm.

Simulations with PL (CTR) and without PL (SES) are conducted with the WRF model in order to verify the impacts of PL on the crossing storm. CTR has successfully reproduced the evolution of the observed storm crossing PL. In CTR, a high  $\theta_{se}$  tongue with center at 850 hPa (which corresponds to the storm) moves eastward and downward, and merges with the LBL induced by the heating and moistening of PL, forming a deep unstable layer under 700 hPa. This deep unstable layer enhances the upward transport of low-level warm and moist air over PL, enhancing the crossing storm. However, in SES, the negative sensible heat flux and small latent heat flux over PL do not produce the LBL, and the convectively stable layer between 925 and 850 hPa is kept, preventing the upward transport of low-level air. This is not conducive to the enhancement of the storm. Besides, the 900-hPa wind difference between CTR and SES shows that a remarkable land–lake breeze circulation and obvious convergence exist over PL, which also contributes to the enhancing of the upward motion. Apparently, the sensitivity experiments further confirm that the destabilization of stable layer between 925 and 850 hPa induced by the heating and moistening of PL and the land–lake breeze jointly strength the storm when it crosses PL.

This study has concentrated on the diagnoses and simulations of the lake-enhanced storm over PL. To forecast the storm better, a further study is needed to probe the favorable environmental conditions (such as the conducive

large-scale circulation, the appropriate lapse rate, the lake–land temperature difference, etc.) in the future. Besides, the impacts of the topography such as the narrow pipe and hills to the southwest of PL and the urban areas around PL also deserve a further in-depth exploration.

**Acknowledgments.** We thank the two anonymous reviewers and the Editor for their constructive comments, which have helped improve this manuscript.

## REFERENCES

- Alcott, T. I., W. J. Steenburgh, and N. F. Laird, 2012: Great Salt Lake-effect precipitation: Observed frequency, characteristics, and associated environmental factors. *Wea. Forecasting*, **27**, 954–971, doi: 10.1175/waf-d-12-00016.1.
- Angel, J. R., and S. A. Isard, 1998: The frequency and intensity of Great Lake cyclones. *J. Climate*, **11**, 61–71, doi: 10.1175/1520-0442(1998)011<0061:tfaiog>2.0.co;2.
- Ballentine, R. J., G. P. Byrd, and T. A. Nizioł, 1993: An operational forecast model for lake-effect snowstorms. Thirteenth Conference on Weather Analysis and Forecasting, Vienna, VA, 2–6 August, Amer. Meteor. Soc., 154–157.
- Barthold, F. E., and D. A. R. Kristovich, 2011: Observations of the cross-lake cloud and snow evolution in a lake-effect snow event. *Mon. Wea. Rev.*, **139**, 2386–2398, doi: 10.1175/mwr-d-10-05001.1.
- Byrd G. P., R. A. Anstett, J. E. Heim, et al., 1991: Mobile sounding observations of lake-effect snowbands in western and central New York. *Mon. Wea. Rev.*, **119**, 2323–2332, doi: 10.1175/1520-0493(1991)119<2323:msoole>2.0.co;2.
- Cao, J. H., X. M. Liu, G. P. Li, et al., 2015: Analysis of the phenomenon of lake–land breeze in Poyang lake area. *Plateau Meteor.*, **34**, 426–435. (in Chinese)
- Carpenter, D. M., 1993: The lake effect of the Great Salt Lake: Overview and forecast problems. *Wea. Forecasting*, **8**, 181–193, doi: 10.1175/1520-0434(1993)008<0181:TLEOTG>2.0.CO;2.
- Dockus, D. A., 1985: Lake effect snow forecasting in the computer age. *Natl. Wea. Dig.*, **10**, 5–19.
- Du, Y., and G. X. Chen, 2019: Heavy rainfall associated with double low-level jets over southern China. Part II: Convection initiation. *Mon. Wea. Rev.*, **147**, 543–565, doi: 10.1175/MWR-D-18-0102.1.
- Fu, M. N., Y. F. Zheng, H. B. Zou, et al., 2013: Analysis on weakening process of convective system passing over Poyang Lake in summer. *Plateau Meteor.*, **32**, 865–873. (in Chinese)
- Grell, G. A., and S. R. Freitas, 2014: A scale and aerosol aware stochastic convective parameterization for weather and air quality modeling. *Atmos. Chem. Phys.*, **14**, 5233–5250, doi: 10.5194/acp-14-5233-2014.
- Gu, H. P., Z. G. Ma, and M. X. Li, 2016: Effect of a large and very shallow lake on local summer precipitation over the Lake Taihu basin in China. *J. Geophys. Res. Atmos.*, **121**, 8832–8848, doi: 10.1002/2015JD024098.
- Hjelmfelt, M. R., 1990: Numerical study of the influence of environmental conditions on lake-effect snowstorms over Lake Michigan. *Mon. Wea. Rev.*, **118**, 138–150, doi: 10.1175/1520-0493(1990)118<0138:NSOTIO>2.0.CO;2.
- Holroyd, E. W. III, 1971: Lake-effect cloud bands as seen from weather satellites. *J. Atmos. Sci.*, **28**, 1165–1170, doi: 10.1175/1520-0469(1971)028<1165:LECBAS>2.0.CO;2.
- Kristovich, D. A. R., and M. L. Spinar, 2005: Diurnal variations in lake-effect precipitation near the western Great Lakes. *J. Hydrometeor.*, **6**, 210–218, doi: 10.1175/JHM403.1.
- Kristovich, D. A. R., L. Bard, and L. Stoecker, 2018: Influence of Lake Erie on a Lake Ontario lake-effect snowstorm. *J. Appl. Meteor. Climatol.*, **57**, 2019–2033, doi: 10.1175/JAMC-D-17-0349.1.
- Laird, N. F., 1999: Observation of coexisting mesoscale lake-effect vortices over the western Great Lakes. *Mon. Wea. Rev.*, **127**, 1137–1141, doi: 10.1175/1520-0493(1999)127<1137:OCMILE>2.0.CO;2.
- Laird, N. F., J. Desrochers, and M. Payer, 2009: Climatology of lake-effect precipitation events over Lake Champlain. *J. Appl. Meteor. Climatol.*, **48**, 232–250, doi: 10.1175/2008JAMC1923.1.
- Laird, N., R. Sobash, and N. Hodas, 2010: Climatological conditions of lake-effect precipitation events associated with the New York State Finger Lakes. *J. Appl. Meteor. Climatol.*, **49**, 1052–1062, doi: 10.1175/2010jamc2312.1.
- Laird, N., A. M. Bentley, S. A. Ganetis, et al., 2016: Climatology of lake-effect precipitation events over Lake Tahoe and Pyramid Lake. *J. Appl. Meteor. Climatol.*, **55**, 297–312, doi: 10.1175/JAMC-D-14-0230.1.
- Lang, C. E., J. M. McDonald, L. Gaudet, et al., 2018: The Influence of a lake-to-lake connection from Lake Huron on the lake-effect snowfall in the vicinity of Lake Ontario. *J. Appl. Meteor. Climatol.*, **57**, 1423–1439, doi: 10.1175/JAMC-D-17-0225.1.
- Li, Y. L., J. Yao, X. L. Zhang, et al., 2017: Study on the vertical stratification in Poyang Lake. *Resour. Environ. Yangtze Basin*, **26**, 915–924, doi: 10.11870/cjlyzyyhj201706014. (in Chinese)
- Liang, X. D., 2007: An integrating velocity–azimuth process single-Doppler radar wind retrieval method. *J. Atmos. Oceanic Technol.*, **24**, 658–665, doi: 10.1175/jtech2047.1.
- Lombardo, K. A., and B. A. Colle, 2012: Ambient conditions associated with the maintenance and decay of quasi-linear convective systems crossing the northeastern U. S. coast. *Mon. Wea. Rev.*, **140**, 3805–3819, doi: 10.1175/MWR-D-12-00050.1.
- Lu, N. P., S. M. Li, N. Zhang, et al., 1988: The calculation of momentum, sensible and latent heat fluxes by bulk transfer method and sodar measurements. Proc. US–PRC International TOGA Symposium, China Ocean Press, Beijing, 251–262.
- Markowski, P., and Y. Richardson, 2010: Mesoscale instabilities. *Mesoscale Meteorology in Midlatitudes*, P. Markowski, and Y. Richardson, Eds., John Wiley & Sons, Ltd, Chichester, West Sussex, UK, 97 pp, doi: 10.1002/9780470682104.ch3.
- McMillen, J. D., and W. J. Steenburgh, 2015: Impact of micro-physics parameterizations on simulations of the 27 October 2010 Great Salt Lake-effect snowstorm. *Wea. Forecasting*, **30**, 136–152, doi: 10.1175/WAF-D-14-00060.1.
- Metz, N. D., 2011: Persistence and dissipation of Lake Michigan-crossing mesoscale convective systems. Ph.D. dissertation, University at Albany, State University of New York, Albany, NY, 237 pp.

- Miner, T. J., and J. M. Fritsch, 1997: Lake-effect rain events. *Mon. Wea. Rev.*, **125**, 3231–3248, doi: 10.1175/1520-0493(1997)125<3231:LERE>2.0.CO;2.
- Moore, P. K., and R. E. Orville, 1990: Lightning characteristics in lake-effect thunderstorms. *Mon. Wea. Rev.*, **118**, 1767–1782, doi: 10.1175/1520-0493(1990)118<1767:LCILET>2.0.CO;2.
- Owens, N. D., R. M. Rauber, B. F. Jewett, et al., 2017: The contribution of lake enhancement to extreme snowfall within the Chicago–Milwaukee urban corridor during the 2011 Groundhog Day blizzard. *Mon. Wea. Rev.*, **145**, 2405–2420, doi: 10.1175/mwr-d-17-0025.1.
- Payer, M., J. Desrochers, and N. F. Laird, 2007: A lake-effect snowband over Lake Champlain. *Mon. Wea. Rev.*, **135**, 3895–3900, doi: 10.1175/2007mwr2031.1.
- Petterssen, S., and P. A. Calabrese, 1959: On some weather influences due to warming of the air by the Great Lakes in winter. *J. Meteor.*, **16**, 646–652, doi: 10.1175/1520-0469(1959)016<0646:OSWIDT>2.0.CO;2.
- Rodriguez, Y., D. A. R. Kristovich, and M. R. Hjelmfelt, 2007: Lake-to-lake cloud bands: Frequencies and locations. *Mon. Wea. Rev.*, **135**, 4202–4213, doi: 10.1175/2007mwr1960.1.
- Rose, B. L. Jr., 2001: The role of upstream lakes in determining downstream severe lake-effect snowstorms. Ph.D. dissertation, University of Illinois at Urbana–Champaign, Champaign, 182 pp.
- Ruhf, R. J., and E. M. C. Cutrim, 2003: Time series analysis of 20 years of hourly precipitation in southwest Michigan. *J. Great Lakes Res.*, **29**, 256–267, doi: 10.1016/s0380-1330(03)70431-6.
- Schoenberger, L. M., 1986: Mesoscale features of the Michigan land breeze using PAM II temperature data. *Wea. Forecasting*, **1**, 127–135, doi: 10.1175/1520-0434(1986)001<0127:MFOTML>2.0.CO;2.
- Schroeder, J. J., D. A. R. Kristovich, and M. R. Hjelmfelt, 2006: Boundary layer and microphysical influences of natural cloud seeding on a lake-effect snowstorm. *Mon. Wea. Rev.*, **134**, 1842–1858, doi: 10.1175/mwr3151.1.
- Shankman, D., B. D. Keim, T. Nakayama, et al., 2012: Hydroclimate analysis of severe floods in China's Poyang Lake region. *Earth Interactions*, **16**, 1–16, doi: 10.1175/2012EI000455.1.
- Slemmer, J. W., 1998: Characteristics of winter snowstorms near Salt Lake City as deduced from surface and radar observations. Master dissertation, Dept. of Meteorology, University of Utah, Utah, 138 pp.
- Steenburgh, W. J., S. F. Halvorson, and D. J. Onton, 2000: Climatology of lake-effect snowstorms of the Great Salt Lake. *Mon. Wea. Rev.*, **128**, 709–727, doi: 10.1175/1520-0493(2000)128<709:COLESO>2.0.CO;2.
- Wan, J. S., D. M. Lyu, and F. J. Liu, 1994: Summer temperature field and its temperature effect in Poyang Lake. *Quart. J. Appl. Meteorol.*, **5**, 374–379. (in Chinese)
- Wang, J. H., Y. Y. Yang, C. S. Miao, et al., 2017: The numerical study of terrain dynamic influence on warm area heavy rainfall of convergence lines in South China coast. *Chinese J. Atmos. Sci.*, **41**, 784–796, doi: 10.3878/j.issn.1006-9895.1702.16182. (in Chinese)
- Wang, R. Q., X. M. Liu, and W. D. Guo, 2016: Observation analyses of the lake–land–atmosphere interaction in Poyang Lake region. *J. Trop. Meteorol.*, **32**, 558–569, doi: 10.16032/j.issn.1004-4965.2016.04.013. (in Chinese)
- Wiggin, B. L., 1950: Great snowstorms of the Great Lakes. *Weatherwise*, **3**, 123–126, doi: 10.1080/00431672.1950.9927065.
- Workoff, T. E., D. A. R., Kristovich, N. F. Laird, et al., 2012: Influence of the Lake Erie overlake boundary layer on deep convective storm evolution. *Wea. Forecasting*, **27**, 1279–1289, doi: 10.1175/WAF-D-11-00076.1.
- Wright, D. M., D. J. Posselt, and A. L. Steiner, 2013: Sensitivity of lake-effect snowfall to lake ice cover and temperature in the Great Lakes Region. *Mon. Wea. Rev.*, **141**, 670–689, doi: 10.1175/MWR-D-12-00038.1.
- Wu, S. S., H. B. Zou, and J. S. Shan, 2018: The effects of different cumulus parameterizations and microphysics schemes in WRF on Typhoon Matmo track after landing. *Torr. Rain Disas.*, **37**, 41–47, doi: 10.3969/j.issn.1004-9045.2018.01.006. (in Chinese)
- Xiao, Y. J., L. P. Liu, and Y. Shi, 2008: Study of methods for three-dimensional multiple-radar reflectivity mosaics. *Acta Meteor. Sinica*, **22**, 351–361.
- Xu, A. H., Z. C. Ye, L. C. Ouyang, et al., 2006: The diagnostic analysis of the track and precipitation of Typhoon “Rananim” after landfall. *J. Trop. Meteorol.*, **22**, 229–236, doi: 10.3969/j.issn.1004-4965.2006.03.004. (in Chinese)
- Xu, H. S., and X. F. Ouyang, 1989: The water temperature of Poyang Lake. *Oceanologia et Limnologia Sinica*, **20**, 343–353. (in Chinese)
- Zou, H. B., S. W. Zhang, X. D. Liang, et al., 2018: Improved algorithms for removing isolated non-meteorological echoes and ground clutters in CINRAD. *J. Meteor. Res.*, **32**, 584–597, doi: 10.1007/s13351-018-7176-9.
- Zou, H. B., S. S. Wu, J. S. Shan, et al., 2019: A method of radar echo extrapolation based on TREC and Barnes filter. *J. Atmos. Oceanic Technol.*, **36**, 1713–1727, doi: 10.1175/JTECH-D-18-0194.1.